AIAA 80-0383bR

Improved Calculation of High Speed Inlet Flows. Part II: Results

Doyle D. Knight*
Rutgers University, New Brunswick, N.J.

An improved numerical algorithm that solves the full mean compressible Navier-Stokes equations has been applied to the calculation of the flowfield in three separate configurations of a simulated high speed aircraft inlet. The inlet geometry consists of a converging supersonic diffuser, formed by two nonparallel plates, followed by a constant height "throat." For all cases, the freestream Mach number is 3.51, and the Reynolds number is 13.6×10^6 based on the inlet length. The three configurations are characterized by different values of the angle of the converging supersonic diffuser and different boundary-layer bleed schedules. The computed results are compared with detailed experimental data for the ramp and cowl surface pressure distribution, and the boundary-layer pitot profiles at seven different streamwise locations. The agreement with the experimental results is generally good, although the experimental data display evidence of three dimensionality over a portion of the inlet flowfield.

Nomenclature

$\dot{m}$ = bleed mass flux, $=\rho_w v_w$
M = Mach number
N = modification to Van Driest damping factor due to bleed
p = static pressure
p_p = pitot pressure
p_t = total pressure
u_* = friction velocity, $=\sqrt{\tau_w/\rho_w}$
U_∞ = freestream velocity
v = velocity normal to wall
x,y = Cartesian coordinates
Δx = mesh spacing in x direction
y'_m = height of computational sublayer
Δy_{SL} = mesh spacing in computational sublayer
δ = boundary-layer thickness
δ_c = cowl angle
ζ,η = transformed coordinates
ν = kinematic viscosity
ρ = density
τ_w = wall shear stress

Subscripts

w = evaluated at wall
∞ = evaluated in freestream

Introduction

An improved numerical algorithm has been developed for the calculation of the flowfield in two-dimensional high speed inlets using the Navier-Stokes equations, with turbulence represented by an algebraic turbulent eddy viscosity.[1] A curvilinear body-oriented coordinate system is employed to handle the arbitrary inlet contours. Provision is included for the general specification of boundary-layer bleed on the ramp and cowl surfaces. The accuracy and improved efficiency of the numerical algorithm was demonstrated for the specific cases of the development of an adiabatic flat plate turbulent boundary layer and the interaction of a shock wave with a turbulent boundary layer.[1,1]

Received Nov. 15, 1979; presented as part of Paper 80-0383 at the AIAA 18th Aerospace Sciences Meeting, Pasadena, Calif., Jan. 14-16, 1980; revision received June 20, 1980.

*Assistant Professor, Dept. of Mechanical, Industrial and Aerospace Engineering. Member AIAA.

In the present paper, the numerical algorithm is applied to the calculation of the flowfield in three different configurations of a simulated high speed inlet. For details of the numerical algorithm, see Ref. 1.

Description of High Speed Inlet

The configuration chosen for study is the two-dimensional high speed inlet investigated by Carter and Spong[2] of the McDonnell Aircraft Company (MCAIR). As illustrated schematically in Fig. 1, the model consists of a converging supersonic diffuser formed by two nonparallel plates followed by a constant-height "throat." The upper and lower surfaces are analogous to the ramp and cowl, respectively, of a high speed inlet. An oblique shock wave train is formed in the converging section of the model, which interacts with the turbulent boundary layer on the ramp and cowl. The distance from the ramp leading edge to the inlet entrance (i.e., the cowl leading edge) is 38.1 cm (15 in.), and the cowl plate is hinged at $x=63.5$ cm (25 in.) to permit variation of the cowl angle δ_c. The height of the throat is controlled by mechanical translation of the ramp plate assembly. Boundary-layer bleed is provided on the ramp and cowl surfaces by means of removable porous plates characterized by discrete arrays of 0.0813 cm (0.032 in.) diam holes oriented normal to the plate surface. The porosity of the plates varies between zero (i.e., solid wall) and 10%. Three separate bleed zones are provided on both the cowl and ramp surfaces. Additional boundary-layer bleed was provided on the inlet sidewalls.

A total of three different configurations were considered in the present effort, corresponding to nominal cowl angles δ_c equal to 6, 8, and 10 deg. In each case, the freestream Mach number M_∞ equals 3.51, and the freestream stagnation temperature and pressure are 322.8 K (581°R) and 340.6 kPa (49.4 psia), respectively, corresponding to a Reynolds number of 1.36×10^7 based on the total inlet length of 78.7 cm (31 in.). The details of the surface bleed are given in Tables 1 and 2, where $\dot{m}$ is the bleed mass flux at the wall (assumed uniform within each bleed zone, with boundary-layer bleed implying negative values of $\dot{m}$) and U_∞ is the freestream velocity upstream of the inlet entrance.

The experimental data consist of ramp and cowl static pressure measurements and boundary-layer pitot profiles at various streamwise locations within the inlet. The static pressure taps were all located on the duct centerline, with the exception of two additional off centerline taps each at $x=43.2$, 57.8, and 66.0 cm (17, 22.75, and 26 in.) on the ramp. There were two pitot rakes each at five stations on the

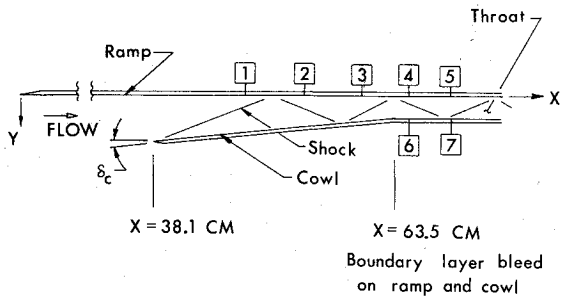

Fig. 1 Geometry of high speed inlet.

ramp (denoted by the symbols o and □ in the figures), positioned off the duct centerline. The general location of these rakes is indicated by the numbers 1-5 in Fig. 1. As illustrated, the rakes are generally positioned upstream and downstream of the shock/boundary-layer interactions on the ramp. The rake pairs at stations 1-3 were attached to the movable bleed plenum separators, while all remaining rakes were fixed in the duct. On the cowl, there were single fixed rakes located off centerline at stations 6 and 7.

Details of Calculation

The calculations were performed in two separate phases. First, the region upstream of the inlet entrance was computed using two overlapping computational regions. Each region contained 48 points in the streamwise x direction, 30 ordinary mesh points in the y direction, and 10 mesh points in the computational sublayer on the ramp.[1] These calculations provided the upstream profiles at $x = 35.3$ cm (13.9 in.) ahead of the inlet entrance for use in computing the three separate inlet configurations. Second, each inlet flowfield was computed using a succession of overlapping computational regions.[3] The number of overlapping regions was two for $\delta_c = 6$ deg, four for $\delta_c = 8$ deg and three for $\delta_c = 10$ deg. Each of the computational regions employed 40 points in the streamwise x direction, 48 ordinary mesh points in the cross-streamwise direction, and 20 points each in computational sublayers on the ramp and cowl.[3] The mesh distributions were obtained from Eq. (1) of Ref. 1. The physical mesh spacing Δx in the streamwise direction was constant in each region. The coordinate transformation technique is not limited to the relatively simple geometry of Fig. 1, and the capability of handling arbitrary curvilinear inlet geometries has been demonstrated.[4] The details of the mesh distributions are indicated in Table 3, where IL is the total number of points in the x direction (overlapped points have been counted only once), JL is the number of ordinary mesh points in the cross-streamwise direction, and JSL0 and JSL1 are the number of points in the computational sublayer (CSL) on the ramp and cowl, respectively. The term max $y_m'^+$ is the maximum value of $y_m' u_*/\nu_w$ taken over all points on the ramp and cowl,[1] and max Δy_{SL}^+ is the corresponding maximum value of $\Delta y_{SL}\, u_* N/\nu_w$, where N is defined in Eq. (5) of Ref. 1.

Table 1 Ramp boundary-layer bleed configurations

δ_c, deg	Bleed zone	Region, cm	$\dot{m}/\rho_\infty U_\infty$
6		No ramp bleed	
8	1	$41.9 \le x \le 52.1$	−0.0054
	2	$52.1 \le x \le 63.5$	−0.0115
	3	$63.5 \le x \le 67.3$	−0.0195
10	1	$41.9 \le x \le 52.7$	−0.0056
	2	$52.7 \le x \le 63.5$	−0.0155
	3	$63.5 \le x \le 67.3$	−0.0255

Table 2 Cowl boundary-layer bleed configurations

δ_c, deg	Bleed zone	Region, cm	$\dot{m}/\rho_\infty U_\infty$
6	1	$55.9 \le x \le 58.4$	−0.0082
	2	$58.4 \le x \le 63.5$	−0.0081
8	1	$49.5 \le x \le 58.7$	−0.0040
	2	$58.7 \le x \le 63.5$	−0.0112
	3	$65.4 \le x \le 67.3$	−0.0139
10	1	$49.2 \le x \le 58.8$	−0.0047
	2	$58.8 \le x \le 63.2$	−0.0146
	3	$65.4 \le x \le 67.3$	−0.0223

As indicated in Table 3, sufficient resolution was provided by the CSL mesh to insure that the first rows of mesh points above the walls were included within the viscous sublayer ($y u_* N/\nu_w \le 5$). The criterion of Eq. (17) of Ref. 1 concerning the height of the sublayer region on the ramp and cowl is met at nearly all positions. The data in Table 3 indicate that y_m' exceeded $60\nu_w/u_*$ at some locations for certain cases. However, based on the rather conservative nature of the criterion, the calculations can all be deemed acceptable. The number of ordinary mesh points within each boundary layer varied between 15 and 20 points.

The streamwise mesh spacing Δx is required to be sufficiently fine to resolve the boundary-layer development, particularly within regions of shock/boundary-layer interaction. The shock-capturing nature of MacCormack's algorithm implies that shock waves are "smeared" over several mesh points, and thus the streamwise mesh spacing furthermore must be sufficiently fine to prevent loss of clarity in the shock wave pattern. No precise criterion exists for the determination of Δx. A commonly accepted approximate criterion for flows with shock/boundary-layer interaction is based on the ratio $\Delta x/\delta$, where δ is the boundary-layer thickness immediately upstream of the shock/boundary-layer interaction. Typical values of $\Delta x/\delta$ range from 0.25 to 1.7, depending on the particular flow problem,[5-10] with $\Delta x/\delta$ generally less than 0.5 for flows with separation. In the present study, flow separation was not observed in any of the cases, due in general to the presence of substantial boundary-layer bleed. The values of $\Delta x/\delta$ for all shock/boundary-layer interactions on the ramp were less than 1.0. On the cowl, the values of $\Delta x/\delta$ were less than 2.0 and 1.6, respectively, for $\delta_c = 6$ and 8 deg, and smaller than 1.0 for $\delta_c = 10$ deg.

The convergence criterion employed is based on the total time of integration of the flowfield.[4] As indicated in Table 4, the total physical time of integration of the flow within each computational region was typically 2.7 t_c, where t_c is the time required for a fluid particle in the inviscid portion of the flow to travel from the upstream to the downstream end of the computational region. The total physical time of typically 2.7 t_c was sufficiently large to insure convergence to steady state. In particular, the maximum relative change in the surface pressure and skin friction distributions over the final physical time period of 0.5 t_c (which typically corresponds to between 40 and 100 time steps in the coarse mesh) was less than 2%. Previous experience by the author in computing strong viscous-inviscid interactions in internal flows indicates that the surface skin friction distribution converges slowest to steady state, and thus monitoring its convergence assures convergence of the flowfield to steady state. The total physical time required for the upstream region was only 2.2 t_c due to the absence of any shock/boundary-layer interaction in the region. The computer time required for each case (using a CDC CYBER 175 computer with FTN Opt. = 1 compiler) is indicated in Table 4. The average number of time steps in the coarse mesh (i.e., region 3 of Fig. 3 in Ref. 1) for each computational region is also shown.

The performance of the numerical algorithm represents an estimated decrease in computer time by a factor of 9 compared to the previous high speed inlet algorithm.[4] This im-

Table 3 Mesh distribution for high speed inlets[a]

Case	IL	JL	JSL0	JSL1	Δx, cm	Max $y_m'^+$	Max Δy_{SL}^+
Upstream	86	30	10	—	0.64	19.8	2.2
$\delta_c = 6$ deg	70	48	10	15	0.64	78.9	5.7
$\delta_c = 8$ deg	123	48	20	20	0.32	82.3	2.3
$\delta_c = 10$ deg	105	48	20	20	0.32[b]	44.1	1.9

[a] See Ref. 1 for definition of terms. [b] $\Delta x = 0.64$ cm used for $35.3 \le x \le 54.9$ cm.

Table 4 Computer times for high speed inlet

Case	t/t_c	Computer time on CYBER 175, h	Average number of time steps in coarse mesh
Upstream	2.2	0.6	235
$\delta_c = 6$ deg	2.7	1.7	513
$\delta_c = 8$ deg	2.7	2.0	221
$\delta_c = 10$ deg	2.9	4.0	413

provement in efficiency is attributable primarily to the use of the CSL modification, operator splitting, and mesh splitting.[1]

The calculations for the $\delta_c = 6$ deg cases were performed twice, using 32-bit, single-precision arithmetic on an IBM 370/168 and 60-bit arithmetic on a CYBER 175. The computed results were virtually identical. For example, the maximum difference in the ramp or cowl pressure distributions between the two calculations is 1%. This result implies that the numerical algorithm is capable of taking advantage of the improved efficiency afforded by the 32-bit arithmetic capability of such machines as the vector-processing CDC STAR 100. Earlier calculations on the CDC STAR using MacCormack's method with both 32-bit and 64-bit arithmetic have provided similar verification.[11]

Results for $\delta_c = 6$ deg

The inlet height for the $\delta_c = 6$ deg configuration varies from 4.67 cm (1.84 in.) at the inlet entrance ($x = 38.1$ cm) to 2.02 cm (0.796 in.) at the inlet throat ($x > 63.5$ cm). As indicated in Tables 1 and 2, boundary-layer bleed is provided only on the cowl, with a total bleed flow (excluding sidewall bleed) of 1.5% of the inlet mass flow. Due to the lack of previous experience of the turbulent eddy viscosity relaxation model of Shang and Hankey[5] with shock/boundary-layer interaction in the presence of bleed and multiple successive shock interactions, the relaxation model was applied to the first shock/boundary-layer interaction on the ramp with a relaxation length of 10 δ.

The computed ramp surface pressure is displayed in Fig. 2, together with the experimental data. The oblique shock wavetrain intersects the ramp at three locations, as indicated by the sharp pressure rise in the vicinity of $x = 50.8$, 63.5 and 71.1 cm (20, 25 and 28 in.). Between $x = 66.0$ and 69.9 cm (26 and 27.5 in.) there is substantial decrease in ramp static pressure due to the impingement of the expansion fan emanating from the hinge point at $x = 63.5$ cm (25 in.) on the cowl. In the vicinity of the first shock impingement point (SIP), the agreement is very good. The computed static pressure in the vicinity of the second and third SIP shows strong qualitative agreement with the data, although the peak pressures at $x = 65.3$ and 73.2 cm (25.7 and 28.8 in.) are below the experimental values. The source of this discrepancy is not clear, although two possible explanations may be offered. First, the streamwise mesh spacing Δx may not be sufficiently fine to resolve the shock/boundary-layer interaction at the second and third SIP on the ramp. The value of $\Delta x/\delta$ at these locations is approximately 0.9. However, results for the ramp pressure at the second and third SIP for $\delta_c = 8$ deg, using virtually identical values of $\Delta x/\delta$, display close agreement with the experimental results (see later), which suggests that

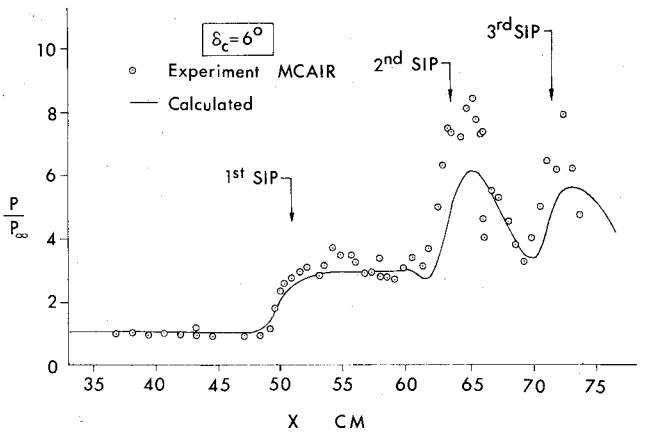

Fig. 2 Static pressure on ramp for $\delta_c = 6$ deg.

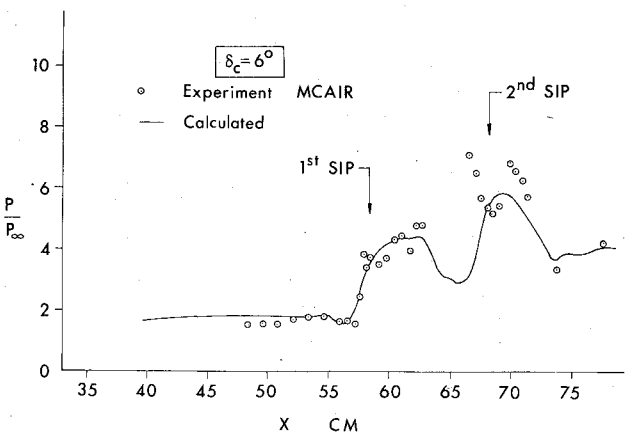

Fig. 3 Static pressure on cowl for $\delta_c = 6$ deg.

the mesh spacing Δx is adequate in the present case. Second, the discrepancy may be due to three-dimensional effects within the experimental flowfield in the vicinity of the second and third SIP. In particular, the static pressure measured by the three spanwise taps at $x = 66.0$ cm (26 in.) varied between 17.7 and 32.4 kPa (2.56 and 4.70 psia).

In Fig. 3, the computed and measured cowl static pressure is shown. The agreement in the vicinity of the first SIP is very good. The computed pressure, however, does not display the double shock structure evident in the experimental data between $x = 66.0$ and 69.9 cm (26.0 and 27.5 in.). The disagreement may be due to three-dimensional effects in the vicinity of the second SIP. This conjecture, however, is not verifiable, as there were no off-centerline static pressure measurements taken on the cowl. The computed pressure downstream of the second SIP is in very good agreement with the data.

The development of the boundary layer on the ramp is indicated in Figs. 4 and 5, which display computed and measured pitot pressure profiles at the five ramp stations. The data from the two pitot rakes located at each station are denoted by the symbols ○ and □, with the pitot pressure p_p

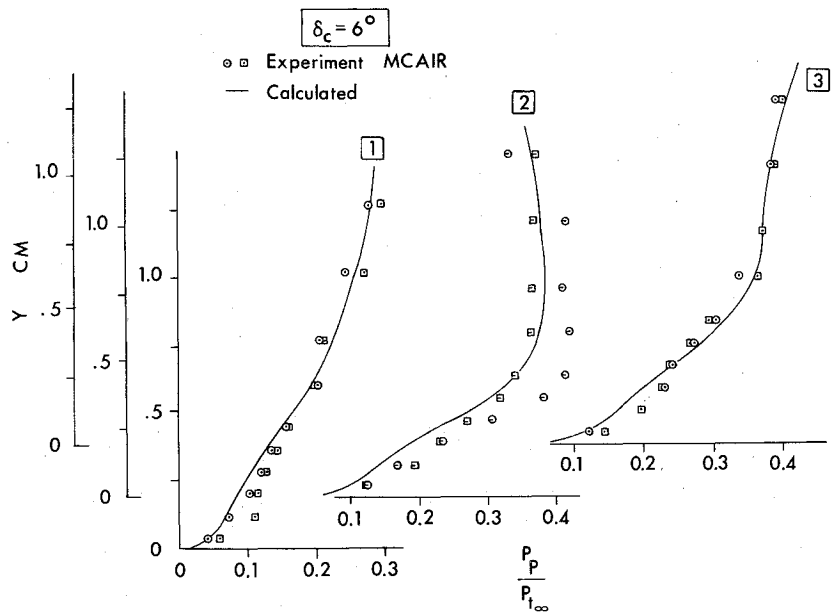

Fig. 4 Pitot pressure profiles on ramp at stations 1-3 for $\delta_c = 6$ deg.

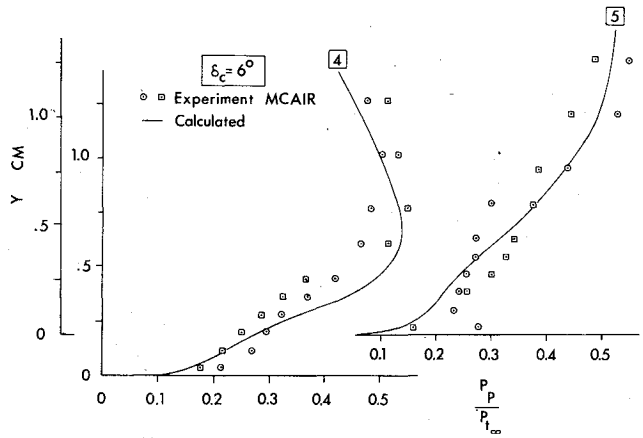

Fig. 5 Pitot pressure profiles on ramp at stations 4 and 5 for $\delta_c = 6$ deg.

nondimensionalized by the freestream total pressure p_{t_∞}. In Fig. 4, results are presented for stations 1-3, corresponding to locations $x = 47.5$, 54.1, and 60.3 cm (18.7, 21.3, and 23.75 in.). As indicated in Figs. 1 and 2, these stations correspond to positions upstream of the first SIP, downstream of the first SIP, and upstream of the second SIP, respectively. The computed profiles are in close agreement with the experimental values. In Fig. 5, results are presented for stations 4 and 5, which correspond to locations $x = 65.4$ and 69.9 cm (25.75 and 27.5 in.) on the ramp. As indicated in Figs. 1 and 2, these stations correspond to positions downstream of the second SIP and upstream of the third SIP, respectively. The computed results at station 4 display generally good agreement with the experimental data except in the outer portion of the boundary layer (0.25 cm $< y <$ 0.50 cm) where the computed pitot pressure is roughly 20% higher. This discrepancy may be due to the existence of significant three-dimensional effects in the vicinity of the second SIP, as discussed earlier. The computed results at station 5 display good agreement with the data.

The development of the boundary layer on the cowl is indicated in Fig. 6, which displays pitot pressure results at stations 6 and 7 corresponding to locations $x = 65.4$ and 69.9 cm (25.75 and 27.5 in.). In this figure, y is measured from the cowl surface. As indicated in Figs. 1 and 3, these stations correspond to positions upstream and slightly downstream of the second SIP on the cowl. The computed results at station 6 are in marked disagreement with the data in the region 0.25 cm $< y <$ 0.5 cm, where the experimental results suggest the presence of a reflected shock wave emanating from a point on the cowl upstream of $x = 65.4$ cm (25.75 in.). As discussed previously, the computed cowl pressure does not display the double shock structure apparent in the experimental cowl pressure between $x = 66$ and 69.9 cm (26 and 27.5 in.). The computed cowl pressure displays, instead, a shock wave intersecting the cowl at approximately $x = 66.0$ cm (26.0 in.) downstream of station 6. The disagreement in the pitot pressure at station 6, therefore, is an indication of the difference between the computed and experimental shock wave pattern in the region $x = 66.0$-69.9 cm (26-27.5 in.), which may be due to three-dimensional effects as discussed earlier. The computed results at station 7 are in generally good agreement with the data except in a region immediately outside the boundary layer between $y = 0.25$ and 0.76 cm (0.10 and 0.30 in.) where the computed values are 10-20% higher.

Results for $\delta_c = 8$ deg

The inlet height for the $\delta_c = 8$ deg configuration varies from 5.568 cm (2.192 in.) at the inlet entrance to 2.027 cm (0.798 in.) at the inlet throat. Boundary-layer bleed was provided on the ramp and cowl, as indicated in Tables 1 and 2, with a total bleed flow (excluding sidewall bleed) of 6.8% of the inlet mass flow. The turbulent eddy viscosity relaxation model was not employed, for the reasons discussed previously.

The computed and measured ramp static pressures are indicated in Fig. 7. The experimental results downstream of the first SIP are somewhat higher than the calculated values, and display two slight "humps" at approximately $x = 54.6$ and 61.0 cm (21.5 and 24 in.). The cause of this discrepancy is not clear. A similar though less pronounced hump is apparent in the $\delta_c = 6$ deg case at a similar location. In the vicinity of the second SIP, the computed results are in close agreement with the data, with the computed peak pressure within 3% of the measured value. Finally, the computed peak pressure at the third SIP is 16% too low, and is shifted approximately 1.3 cm (0.5 in.) downstream. This small displacement of the shock structure, observable to a much smaller degree at the second SIP, is possibly due to the inherent "smearing" of the shock wave structure by the numerical algorithm, and suggests that a smaller $\Delta x/\delta$ may be desirable in the vicinity of the third SIP.

In Fig. 8, the computed and measured cowl pressures are displayed. Between $x = 47.0$ and 55.9 cm (18.5 and 22 in.), the

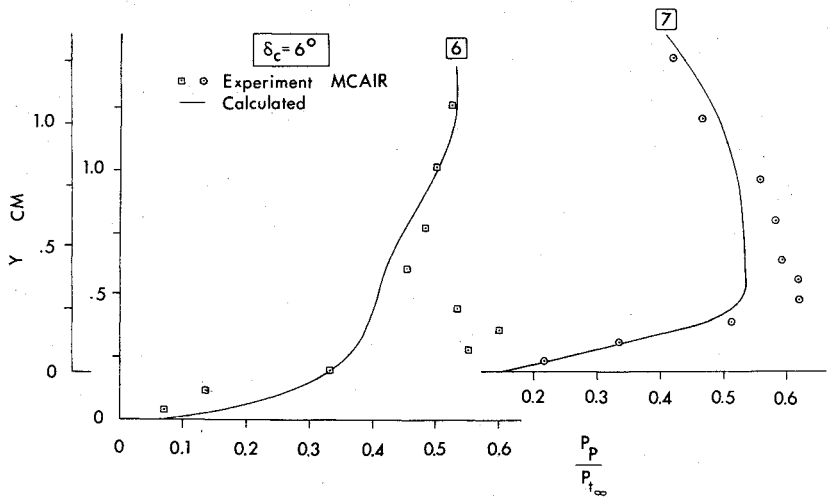

Fig. 6 Pitot pressure profiles on cowl at stations 6 and 7 for $\delta_c = 6$ deg.

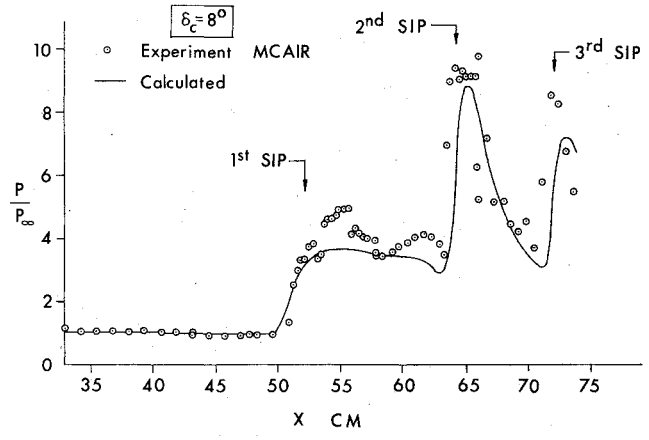

Fig. 7 Static pressure on ramp for $\delta_c = 8$ deg.

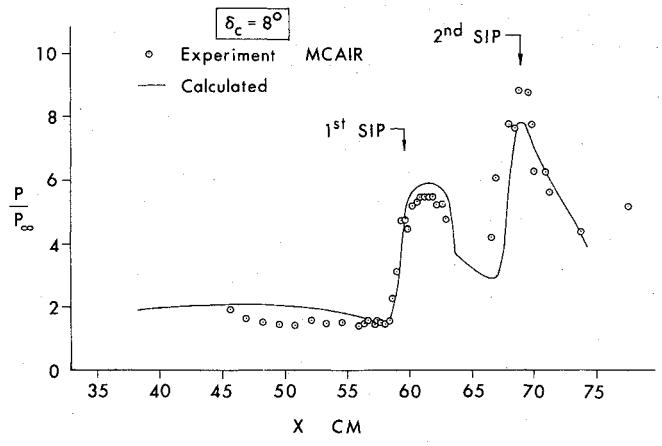

Fig. 8 Static pressure on cowl for $\delta_c = 8$ deg.

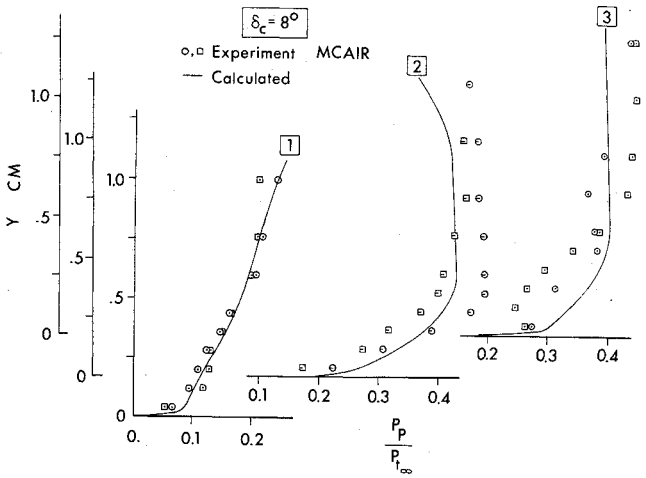

Fig. 9 Pitot pressure profiles on ramp at stations 1-3 for $\delta_c = 8$ deg.

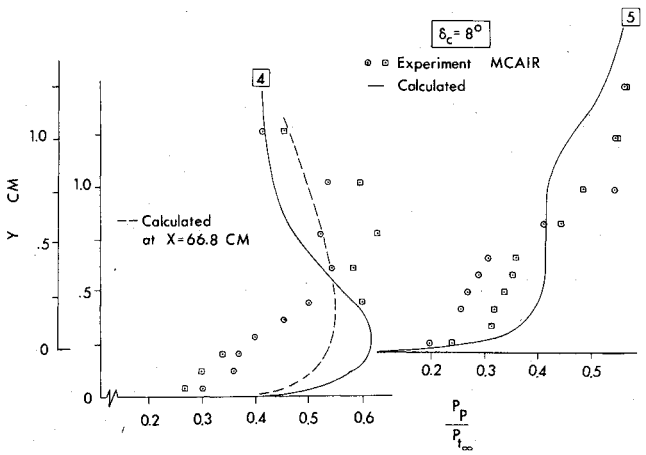

Fig. 10 Pitot pressure profiles on ramp at stations 4 and 5 for $\delta_c = 8$ deg.

observed pressures are 10-25% below the computed values. However, within the portion of this region that is coincident with cowl bleed zone 1 (i.e., $x = 49.5$-55.9 cm, shown in Table 2), the experimental data indicate that the cowl surface pressure is slightly less than the pressure within the bleed plenum beneath the surface, suggesting the possibility of negative bleed flow (i.e., surface blowing) in this region, that may account for the discrepancy in cowl pressure. The computed results for the first SIP are in close agreement with the data, with the maximum pressure predicted within 4%. At the second SIP, the computed peak pressure is 11% below the experimental value.

The ramp boundary-layer development is indicated in Figs. 9 and 10. The pitot pressure results for stations 1-3, corresponding to locations $x = 48.8$, 55.4, and 61.0 cm (19.2, 21.8, and 24 in.), are displayed in Fig. 9. As indicated in Figs. 1 and 7, these stations correspond to positions upstream of the first SIP, downstream of the first SIP, and upstream of the second SIP, respectively. The computed results are in generally good agreement with the experimental data. In Fig. 10, pitot pressure results are displayed for stations 4 and 5,

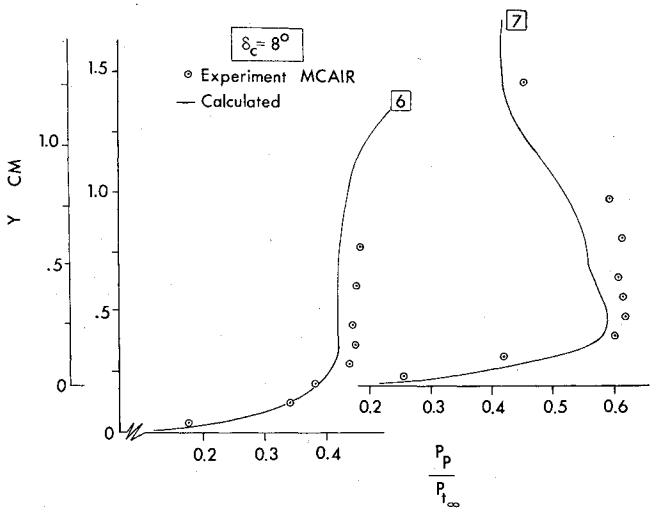

Fig. 11 Pitot pressure profiles on cowl at stations 6 and 7 for $\delta_c = 8$ deg.

corresponding to positions $x = 65.4$ and 69.6 cm (25.75 and 27.5 in.), which are located downstream of the second SIP and upstream of the third SIP, respectively. The computed results at station 4 for y less than 0.64 cm (0.25 in.) are in substantial disagreement with the data. A substantial spanwise variation in measured ramp static pressure is evident in Fig. 7 at $x = 66.0$ cm (26 in.), with values ranging from 23.0 and 27.4 kPa (3.34 and 3.97 psia) at the off-centerline taps to 43.0 kPa (6.24 psia) on the centerline. This three-dimensional character may be partially due to a spanwise curvature in the shape of the shock wave intersecting the ramp at the second SIP, which may arise from slight spanwise variations in the duct height.[12] This interpretation implies, from Fig. 7, that the shock is curved slightly upstream. Noting that the pitot rakes are located off centerline, this suggests comparison of the data with the computed pitot pressure at a point slightly downstream of station 4. As a rough estimate, therefore, computed results at $x = 66.8$ cm (26.3 in.) are also indicated, and demonstrate a better trend in comparison with the data. There remains substantial disagreement, however. Judging from the abrupt nature of the pressure rise at the second SIP, this disagreement may be attributable to the limitations of the turbulent eddy viscosity model.[1] The pitot pressure at station 5 displays an incoming shock wave at approximately $y = 1.0$ cm (0.4 in.) that is slightly above the location $y = 0.64$ cm (0.25 in.) apparent in the experimental data. This discrepancy is further evidence of the slight downstream displacement of the computed shock structure in the vicinity of the third SIP, as discussed previously.

The boundary-layer development on the cowl is displayed in Fig. 11, which indicates the pitot pressure results at stations 6 and 7 corresponding to locations $x = 65.4$ and 69.9 cm (25.75 and 27.5 in.) positioned upstream and downstream of the second SIP on the cowl. The distance y is measured from the cowl surface. The computed profiles at stations 6 and 7 are within 7 and 12% of the data, respectively.

In order to evaluate the effect of the assumptions employed in the CSL modification, the correction to the computed wall shear stress on the ramp and cowl was evaluated from Eq. (19) of Ref. 1. The average of the absolute percentage correction was found to be 1.2%, thus supporting the validity of the CSL modification. In determining this quantity, those pairs of mesh points between which the bleed mass flux changes discontinuously (see Tables 1 and 2) in general have been omitted. Naturally, at these points the assumption of negligible streamwise variation in the mass, momentum, and enthalpy fluxes[1] is invalid. However, these points account for only 3.1% of the total number of mesh points on the ramp and cowl, and therefore the effect on the flowfield is quite small.

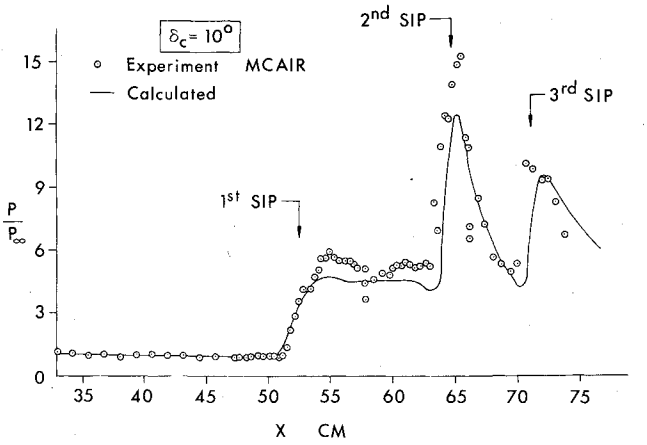

Fig. 12 Static pressure on ramp for $\delta_c = 10$ deg.

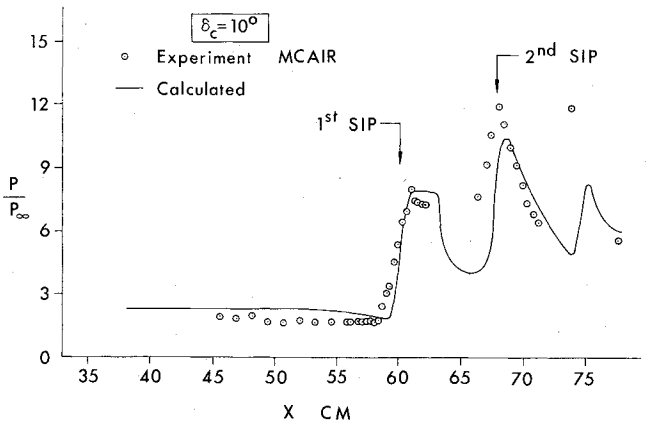

Fig. 13 Static pressure on cowl for $\delta_c = 10$ deg.

Results for $\delta_c = 10$ deg

The inlet height for the $\delta_c = 10$ deg configuration varies from 6.469 cm (2.547 in.) at the inlet entrance to 2.024 cm (0.797 in.) at the inlet throat. As indicated in Tables 1 and 2, boundary-layer bleed was provided on the ramp and cowl, with a total bleed flow (excluding sidewall bleed) of 7.4% of the inlet mass flow. As in the $\delta_c = 8$ deg case, the turbulent eddy viscosity relaxation model was not employed.

The computed and measured ramp static pressure are displayed in Fig. 12. The agreement in the vicinity of the first SIP is very good. The computed downstream plateau pressure is typically 14% below the experimental centerline measurements, although within the spanwise variation evident at $x = 57.8$ cm (22.75 in.). The computed results in the vicinity of the second SIP are in close agreement with the data, although the peak pressure is 18% too low. Judging from the exceptionally abrupt pressure rise, it is possible that a finer streamwise mesh spacing is needed in this region. The computed pressure profile at the third SIP is displayed slightly downstream of the data in a manner similar to the $\delta_c = 8$ deg case. The peak pressure is within 5% of the measured value.

The computed and measured cowl pressure is shown in Fig. 13. Between $x = 49.5$ and 57.2 cm (19.5 and 22.5 in.), the computed pressure is between 24 and 36% above the data. However, within this region the experimental results indicate that the cowl surface pressure is slightly less than the pressure within the bleed plenum underneath the surface, suggesting as in the $\delta_c = 8$ deg case the possibility of negative bleed flow, that may account for the discrepancy in cowl pressure. At the first SIP, the computed pressure is in close agreement with the data. The comparison at the second SIP is also good, with the peak pressures agreeing within 12%. The computed profile also displays the slight characteristic downstream displacement seen previously.

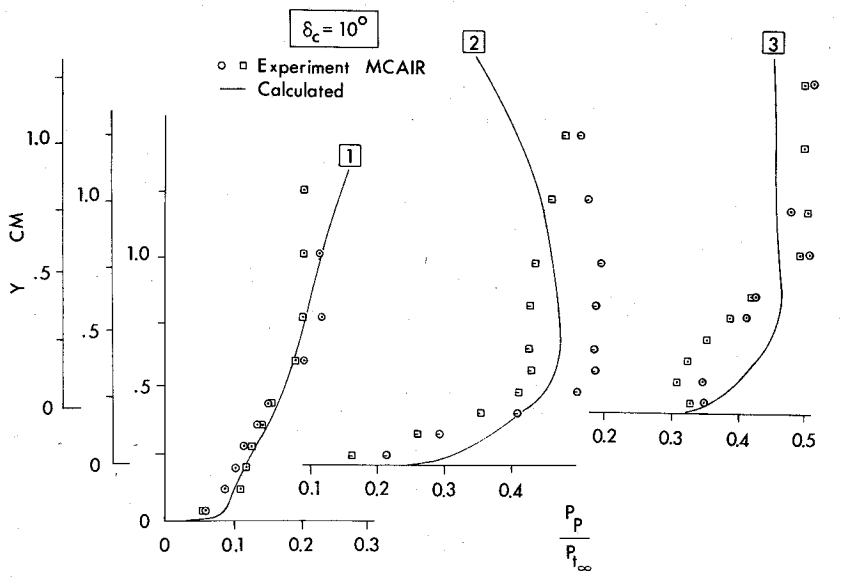

Fig. 14 Pitot pressure profiles on ramp at stations 1-3 for $\delta_c = 10$ deg.

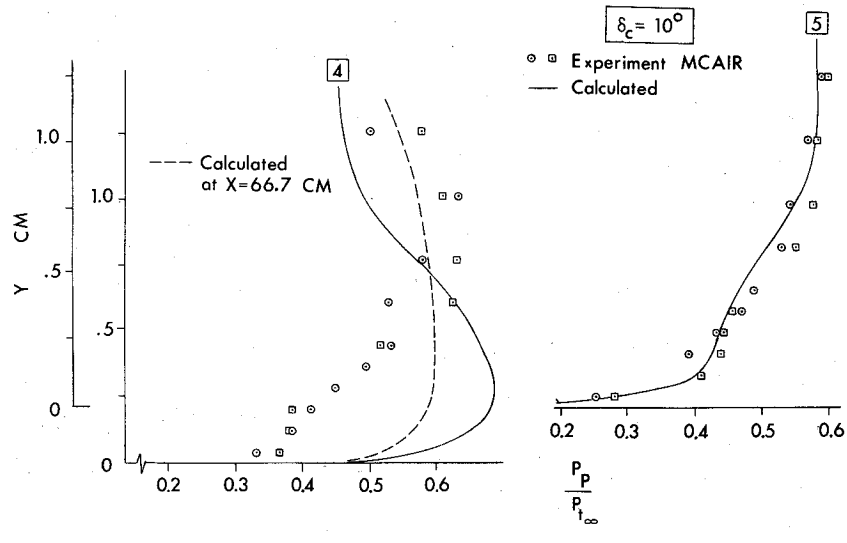

Fig. 15 Pitot pressure profiles on ramp at stations 4 and 5 for $\delta_c = 10$ deg.

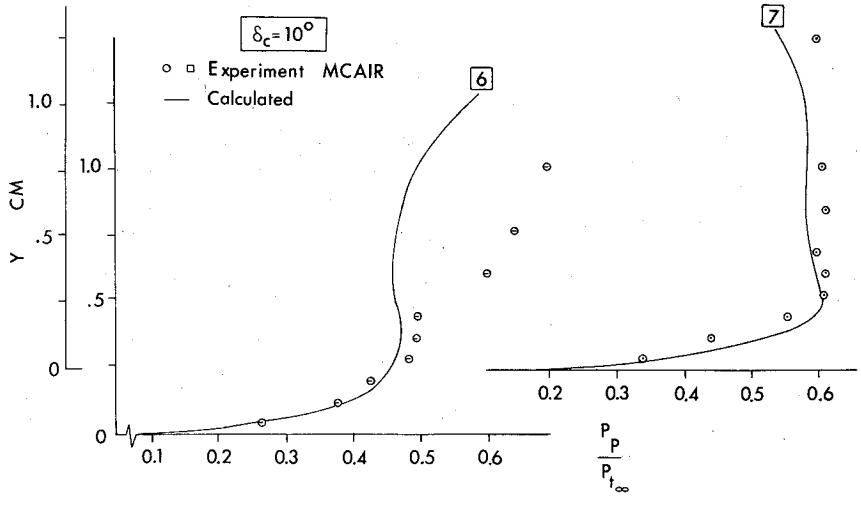

Fig. 16 Pitot pressure profiles on cowl at stations 6 and 7 for $\delta_c = 10$ deg.

The ramp boundary-layer development is shown in Figs. 14 and 15. The pitot pressure results for stations 1-3, corresponding to locations $x = 49.4$, 56.0, and 61.0 cm (19.46, 22.06, and 24.0 in.) are indicated in Fig. 14.

The agreement is good, although the computed profile at station 3 displays a somewhat fuller profile within the boundary layer. In Fig. 15, pitot pressures are shown for stations 4 and 5, corresponding to positions $x = 65.4$ and 69.9 cm (25.75 and 27.5 in.), which are immediately downstream of the second SIP and upstream of the third SIP, respectively. As in the $\delta_c = 8$ deg case, there is substantial disagreement between the computed and measured profiles for y less than

0.64 cm (0.25 in.). The ramp static pressure measurements at $x = 66.0$ cm (26 in.) display a substantial spanwise variation, with values ranging from 28.3 and 31.0 kPa (4.1 and 4.49 psia) at the off-centerline taps to 47.6 kPa (6.90 psia) on the inlet centerline. A similar partial explanation as in the $\delta_c = 8$ deg case may be suggested. For purposes of estimation the computed results at $x = 66.7$ cm (26.25 in.) are presented and they display a closer trend with the data. Nonetheless, substantial disagreement exists, which as in the $\delta_c = 8$ deg case may be attributable to the limitations of the turbulent eddy viscosity model employed. The final pitot profile at station 5 displays excellent agreement with the experimental results.

The cowl boundary-layer development is shown in Fig. 16, where computed and measured pitot profiles are displayed for stations 6 and 7 corresponding to locations $x = 65.4$ and 69.9 cm (25.75 and 27.5 in.). Within the boundary layer $y < 0.38$ cm (0.15 in.) at station 6, the computed profile is in close agreement with the data, with a maximum discrepancy of 4%. Outside the boundary layer, the computed profile indicates an incoming shock at approximately 1.27 cm (0.5 in.) from the cowl, which is farther away than the actual shock at approximately $y = 0.56$ cm (0.22 in.). This discrepancy is another indication of the characteristic small downstream displacement of the second SIP on the cowl discussed previously. The final cowl pitot profile at station 7 is seen to be in very good agreement with the data.

The average absolute percentage correction to the wall shear stress was evaluated in the manner discussed previously and found to be 0.74%, thus supporting the validity of the CSL modification. The number of boundary mesh points omitted from this estimate due to their proximity to abrupt changes in the bleed mass flux was 3.1% of the total number of mesh points on the ramp and cowl.

Conclusions

An improved numerical algorithm has been applied to the calculation of the flowfields of three different configurations of a simulated high speed inlet at a Mach number of 3.5 and Reynolds number of 13.6×10^6 based on inlet length. The algorithm solves the Navier-Stokes equations for two-dimensional flow, with turbulence represented by an algebraic turbulent eddy viscosity. Detailed comparison is made with measured wall static pressures and pitot pressure profiles on the ramp and cowl. The agreement with the experimental results is generally good, although the experimental data displayed evidence of three dimensionality over a portion of the inlet flowfield. The computer time for the region upstream of the inlet entrance (common to all configurations) was 0.6 h on a CDC CYBER 175, while the computer time for the inlet internal flowfield varied from 1.7 to 4.0 h depending on the configuration. These results represent an estimated decrease in computer time by a factor of approximately 9 compared to the previous work by the author.

Acknowledgment

This research was performed through sponsorship of the Air Force Flight Dynamics Laboratory under AF Contract F33615-78-C-3008.

References

[1] Knight, D., "Improved Calculation of High Speed Inlet Flows. Part I: Numerical Algorithm," *AIAA Journal*, Vol. 19, Jan. 1981, pp. 34-41.

[2] Carter, T. D. and Spong, E. D., "High Speed Inlet Investigation. Vol. I: Description of Program and Results. Vol. II: Data Summary," AFFDL-TR-77-105, Nov. 1977.

[3] Knight, D., "Calculation of High Speed Inlet Flows Using the Navier-Stokes Equations. Vol. I: Description of Results, Vol. II: User's and Programmer's Guide," AFFDL-TR-79-3138, Feb. 1980.

[4] Knight, D., "Numerical Simulation of Realistic High Speed Inlets Using the Navier-Stokes Equations," *AIAA Journal*, Vol. 15, Nov. 1977, pp. 1583-1589.

[5] Shang, J. and Hankey, W. L. Jr., "Numerical Solution for Supersonic Turbulent Flow Over a Compression Ramp," *AIAA Journal*, Vol. 13, Oct. 1975, pp. 1368-1374.

[6] Shang, J., Hankey, W. L. Jr., and Law, C., "Numerical Simulation of Shock Wave-Turbulent Boundary Layer Interaction," *AIAA Journal*, Vol. 14, Oct. 1976, pp. 1451-1457.

[7] Baldwin, B. and MacCormack, R., "Numerical Solution of the Interaction of a Strong Shock Wave with a Hypersonic Turbulent Boundary Layer," AIAA Paper 74-558, June 1974.

[8] Horstman, C. and Hung, C., "Computation of Three-Dimensional Turbulent Separated Flows at Supersonic Speeds," AIAA Paper 79-0002, Jan. 1979.

[9] Hung, C. and MacCormack, R., "Numerical Solution of Three-Dimensional Shock Wave and Turbulent Boundary Layer Interaction," *AIAA Journal*, Vol. 16, Oct. 1978, pp. 1090-1096.

[10] Rose, W., "Practical Aspects of Using Navier-Stokes Codes for Predicting Separated Flows," AIAA Paper 76-96, Jan. 1976.

[11] Shang, J., Buning, P., Hankey, W. L. Jr., and Wirth, W., "The Performance of a Vectorized 3-D Navier-Stokes Code on the CRAY-1 Computer," *Proceedings of the AIAA Computational Fluid Dynamics Conference*, July 1979, pp. 27-35.

[12] Stava, D., private communication, Air Force Flight Dynamics Laboratory, June 1979.